The Astrophysical Journal, 960:21 (8pp), 2024 January 1 https://doi.org/10.3847/1538-4357/ad06ae


# Gamma-Ray Burst Observations by the High-Energy Particle Detector on board the China Seismo-Electromagnetic Satellite between 2019 and 2021

F. Palma[1], M. Martucci[1], C. Neubüser[2], A. Sotgiu[1], F. M. Follega[2,3], P. Ubertini[4], A. Bazzano[4], J. C. Rodi[4], R. Ammendola[1], D. Badoni[1], S. Bartocci[1], R. Battiston[2,3], S. Beolè[5,6], I. Bertello[4], W. J. Burger[2], D. Campana[7], A. Cicone[8], P. Cipollone[1], S. Coli[6], L. Conti[1,9], A. Contin[10,11], M. Cristoforetti[2,12], G. D'Angelo[4], F. De Angelis[4], C. De Donato[1], C. De Santis[1], P. Diego[4], A. Di Luca[2,12], E. Fiorenza[4], G. Gebbia[2,3], R. Iuppa[2,3], A. Lega[2,3], M. Lolli[11], B. Martino[13], G. Masciantonio[1], M. Mergè[1,14], M. Mese[7,15], A. Morbidini[4], F. Nozzoli[2], F. Nuccilli[4], A. Oliva[11], G. Osteria[7], F. Palmonari[10,11], B. Panico[7,15], E. Papini[4], A. Parmentier[4], S. Perciballi[5,6], F. Perfetto[7], A. Perinelli[2,3], P. Picozza[1,16], M. Piersanti[8], M. Pozzato[11], G. Rebustini[1], D. Recchiuti[4], E. Ricci[2,3], M. Ricci[17], S. B. Ricciarini[18], A. Russi[4], Z. Sahnoun[10,11], U. Savino[5,6], V. Scotti[7,15], X. Shen[19], R. Sparvoli[1,16], S. Tofani[4], N. Vertolli[4], V. Vilona[2], V. Vitale[1], U. Zannoni[4], Z. Zeren[20], S. Zoffoli[14], and P. Zuccon[2,3]
[1] INFN-Sezione di Roma "Tor Vergata", Via della Ricerca Scientifica 1, I-00133 Roma, Italy; francesco.palma@roma2.infn.it
[2] INFN-TIFPA, Via Sommarive 14, I-38123 Povo (Trento), Italy
[3] University of Trento, Via Sommarive 14, I-38123 Povo (Trento), Italy
[4] INAF-IAPS, Via Fosso del Cavaliere 100, I-00133, Roma, Italy
[5] University of Torino, Via P. Giuria 1, I-10125 Torino, Italy
[6] INFN-Sezione di Torino, Via P. Giuria 1, I-10125 Torino, Italy
[7] INFN-Sezione di Napoli, Via Cintia, I-80126, Napoli, Italy
[8] University of L'Aquila, Via Vetoio, I-67100, L'Aquila, Italy
[9] Uninettuno University, Corso V. Emanuele II, 39, I-00186, Roma, Italy
[10] University of Bologna, Viale Berti Pichat 6/2, Bologna, Italy
[11] INFN-Sezione di Bologna, Viale Berti Pichat 6/2, Bologna, Italy
[12] Fondazione Bruno Kessler, Via Sommarive 18, I-38123 Povo (Trento), Italy
[13] CNR, Via Fosso del Cavaliere 100, I-00133, Roma, Italy
[14] Italian Space Agency, Via del Politecnico, I-00133 Roma, Italy
[15] University of Napoli "Federico II", Via Cintia, I-80126, Napoli, Italy
[16] University of Roma "Tor Vergata", Via della Ricerca Scientifica 1, I-00133 Roma, Italy
[17] INFN-LNF, V.E. Fermi, 54, I-00044 Frascati (Roma), Italy
[18] IFAC-CNR, Via Madonna del Piano, 10, I-50019 Sesto Fiorentino (Firenze), Italy
[19] National Space Science Center, Chinese Academy of Sciences, Beijing 100190, People's Republic of China
[20] National Institute of Natural Hazards, Ministry of Emergency Management of China, Beijing 100085, People's Republic of China
*Received 2023 May 25; revised 2023 October 23; accepted 2023 October 23; published 2023 December 19*

## Abstract

In this paper we report the detection of five strong gamma-ray bursts (GRBs) by the High-Energy Particle Detector (HEPD-01) mounted on board the China Seismo-Electromagnetic Satellite, operational since 2018 on a Sun-synchronous polar orbit at a ∼507 km altitude and 97° inclination. HEPD-01 was designed to detect high-energy electrons in the energy range 3–100 MeV, protons in the range 30–300 MeV, and light nuclei in the range 30–300 MeV $n^{-1}$. Nonetheless, Monte Carlo simulations have shown HEPD-01 is sensitive to gamma-ray photons in the energy range 300 keV–50 MeV, even if with a moderate effective area above ∼5 MeV. A dedicated time correlation analysis between GRBs reported in literature and signals from a set of HEPD-01 trigger configuration masks has confirmed the anticipated detector sensitivity to high-energy photons. A comparison between the simultaneous time profiles of HEPD-01 electron fluxes and photons from GRB190114C, GRB190305A, GRB190928A, GRB200826B, and GRB211211A has shown a remarkable similarity, in spite of the different energy ranges. The high-energy response, with peak sensitivity at about 2 MeV, and moderate effective area of the detector in the actual flight configuration explain why these five GRBs, characterized by a fluence above $\sim 3 \times 10^{-5}$ erg $cm^{-2}$ in the energy interval 300 keV–50 MeV, have been detected.

*Unified Astronomy Thesaurus concepts:* Cosmic ray detectors (325); Gamma-ray bursts (629); Particle astrophysics (96)

## 1. Introduction

Cosmic impulsive gamma-ray signals, namely, gamma-ray bursts (GRBs), are extremely intense electromagnetic events detected at the top of the Earth's atmosphere by high-energy photon detectors. GRBs were serendipity discovered in 1967 by the Vela satellites designed to monitor nuclear explosions during the Cold War (Klebesadel et al. 1973). Just after their discovery, it was clear that GRBs were among the most energetic phenomena present in the Universe, and a number of dedicated instruments were built to systematically study them and understand their complex nature. Important progress was made with the launch of the NASA Gamma Ray Observatory (GRO), carrying on board the Burst and Transient Source Experiment (BATSE) all-sky monitor, specifically designed to detect GRBs. For the first time, BATSE provided a wide energy range coverage and high timing resolution (Fishman 2013), discovering important characteristics of GRBs, such as a bimodal time behavior that divides GRBs into

short and long ones, according to their $T_{90}$ time duration (either smaller or larger than 2 s); see Mazets et al. (1981), Dezalay et al. (1991), Kouveliotou et al. (1993), and references therein. $T_{90}$ measures, in seconds, the duration of the time interval during which 90% of the total observed counts have been detected. $T_{90}$ starts after 5% of the total GRB counts have been detected, and ends when the detected GRB counts are 95%. It was also clear that GRB flux was normally peaking at keV energies, usually accompanied by low- and high-energy components (Band et al. 1993). In addition, their isotropic spatial distribution was confirmed, even though GRO was not able to discern whether their nature was galactic or extragalactic. The cosmic origin of GRBs was finally unveiled with the first unambiguous detection of their optical counterpart by the Hubble Space Telescope (van Paradijs et al. 1997), and the discovery of the X-Ray afterglow by the BeppoSAX satellite (Costa et al. 1997). Following these discoveries, ESA promoted the INTEGRAL mission (Winkler et al. 2003), able to detect GRBs in the energy range 3 keV–10 MeV and with arcminute localization, accompanied by gamma-ray all-sky monitoring with 85% efficiency and real-time web GCN (GRB Coordinates Network) alert features (Mereghetti et al. 2003).

Subsequently, NASA approved the Swift satellite program, now renamed Neil Gehrels Swift Observatory (Gehrels et al. 2004) featuring hard X-ray arcminute angular resolution localization, prompt detection by the Burst Alert Telescope (BAT) soft gamma-ray imager, and unprecedented fast re-pointing with follow-up imaging capability by the X-Ray Telescope (XRT). Swift ultraviolet coverage by the Ultraviolet and Optical Telescope helped clarify that GRBs are strong extragalactic explosions, so far detected up to redshift 8.2 (Campana et al. 2022). Short and long GRBs are now known to be generated by very different collapsing processes: the long ones are linked to a particular type of core-collapse (fast-rotating) supernova subset (Galama et al. 1998; Cano et al. 2017). The short ones have been recently confirmed to be generated by binary neutron star mergers, thanks to the simultaneous detection of GW170817 by ground interferometers (Abbott et al. 2017a) and GRB170817A by Fermi and INTEGRAL Observatories (Abbott et al. 2017b; Goldstein et al. 2017; Savchenko et al. 2017; Ubertini et al. 2019). Finally, the hypothesis that at least some GRBs could be generated by giant magnetar flares (Mazets et al. 1979, 2008; Burns et al. 2021; Svinkin et al. 2021) is still debated as shown by Schösser et al. (2023).

A handful of them, the strongest ones, have also shown a gamma-ray afterglow, as also recently confirmed by observations of the so-called Brightest of All Time (BOAT), also known as GRB221009A (see Burns et al. 2023; Rodi & Ubertini 2023; and references therein). Also, this GRB has been observed at an energy greater than 10 TeV by the Large High Altitude Air Shower Observatory detector with an operative energy range of up to 18 TeV (Huang et al. 2022).

GRBs are usually detected using electromagnetic detectors. However, upon the occurrence of GRB221009A, we were able to identify a mechanism that, through the conversions of X and gamma rays, allowed solid-state particle sensors, such as the HEPP-L detector also flying on board the China Seismo-Electromagnetic Satellite (CSES-01; Shen et al. 2018), to accurately detect the most intense part of the BOAT GRB (Battiston et al. 2023). The present study is meant to extend this latter analysis to High-Energy Particle Detector (HEPD-01) data, with the aim to provide additional information on the reported GRBs, and in particular to provide the light curve and fluence in the energy range 300 keV–50 MeV.

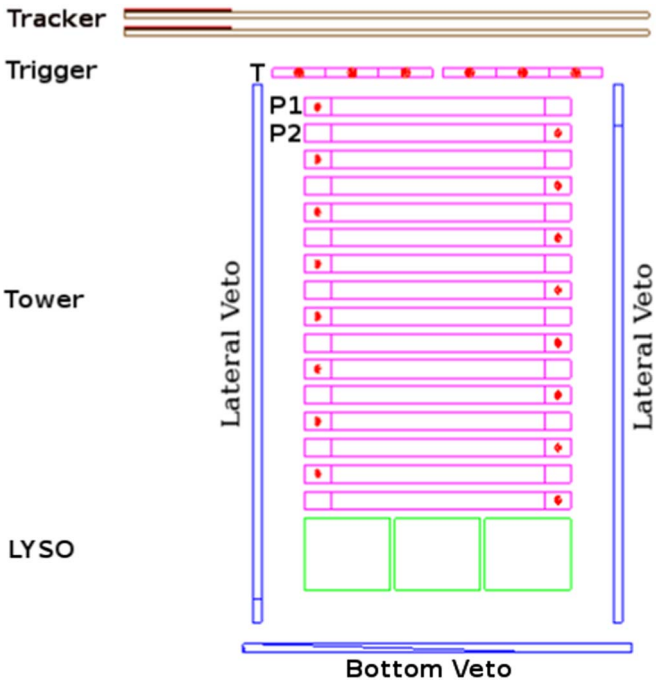


**Figure 1.** Schematic of the HEPD-01 detector. All mechanical structures (as well as the lateral VETO planes located in the front and the back) have been removed from the figure for visualization purposes.

## 2. CSES-01 Mission and the HEPD-01 Detector

CSES-01 is the first item of an extended constellation of Low-Earth Orbit (LEO) satellites, designed for monitoring perturbations of electromagnetic fields and waves, plasma and charged particle fluxes induced by both natural (earthquakes, solar events, cosmic rays, etc.) and anthropogenic sources in the near-Earth space. For these purposes, since 2018 February 2, CSES-01 has been flying on a Sun-synchronous polar orbit at a ∼507 km altitude, a 97° inclination, and a ∼5 day revisiting periodicity.

CSES-01 relies on nine instruments operating between ±70° latitude, as they are usually switched off beyond these values due to adjustments in attitude and additional scheduled maneuvers. One of these payloads is HEPD-01, which was designed and built by the Limadou Collaboration, the Italian portion of the CSES mission. A schematic representation of this compact ($40.36 \times 53.00 \times 38.15$ cm$^3$) and light (∼45 kg) apparatus is depicted in Figure 1.

From top to bottom, HEPD-01 is equipped with the following set of subdetectors: a tracker made up of two double-sided silicon microstrip planes ($213.2 \times 214.8 \times 0.3$ mm$^3$), a trigger system (T) including one EJ-200 plastic scintillator layer segmented into six paddles ($20 \times 3 \times 0.5$ cm$^3$ each), a range calorimeter comprising a tower of 16 plastic scintillator planes, P1, P2, ..., P16 ($15 \times 15 \times 1$ cm$^3$) and a matrix of $3 \times 3$ lutetiumyttrium oxyorthosilicate (LYSO) inorganic scintillator crystals ($5 \times 5 \times 4$ cm$^3$). Finally, the detector is completed by an anti-coincidence (VETO) system composed of five plastic scintillator planes, out of which four are placed at the lateral sides of the apparatus and one at the bottom. The combination of these subdetectors optimizes the detection of electrons and protons in the 3–100 MeV and ∼30–300 MeV

energy ranges, respectively, as well as the measurement of light nuclei, with a $\pm 60^{\circ}$ field of view and a geometrical acceptance of more than 400 $cm^2$ sr.

Since the end of the commissioning phase in August 2018, HEPD-01 has been returning valuable information on galactic protons (Bartocci et al. 2020) and their solar modulation (Martucci et al. 2023), trapped protons in the South Atlantic Anomaly (Martucci et al. 2022), and space weather phenomena, such as geomagnetic storms (Palma et al. 2021; Piersanti et al. 2022) and solar energetic particle events (Martucci et al. 2023). A more detailed description of the HEPD-01 detector can be found in Picozza et al. (2019), Ambrosi et al. (2020), and Ambrosi et al. (2021).

## 3. HEPD-01 Data Acquisition

HEPD-01 spends most of CSES-01 orbit time performing acquisition runs, during which scientific data are acquired only for incoming particles satisfying a single predefined trigger mask configuration. A dedicated command can be transmitted in order to set one of the eight predefined trigger mask configurations (Sotgiu et al. 2021), which are given by different logic combinations of counters from the various subdetectors. Hence, the different trigger masks define the aperture and the energy acceptance of the instrument. For example, the upmost trigger condition, labeled as T, corresponds to an above-threshold signal only in the trigger plane, and it is associated with the lowest energy threshold. By requiring a deeper penetration of the particle inside the detector (i.e., using the trigger plane counters and a set of tower planes in "AND" configuration, such as T & P1 and T & P1 & P2), the geometric factor of HEPD-01 decreases, and consequently, the energy threshold for triggering increases. In the case of electron detection, the energy thresholds resulting from T, T & P1, and T & P1 & P2 trigger conditions are $> 3$ MeV, $> 4.5$ MeV, and $> 8$ MeV, respectively. Moreover, each of these predefined trigger masks can be used with different VETO settings: no veto, lateral veto alone, bottom veto alone, or whole veto (lateral+bottom). At the end of the commissioning phase, following six months of calibration and testing, HEPD-01 was configured with a trigger condition, labeled as T & P1 & P2, which corresponds to event acquisition and processing only when the deposited signals in the trigger plane and the first two calorimeter planes (P1, P2) are above predefined thresholds, consequently constraining the energy of the incoming particles processed during data acquisition. However, for each of the eight predefined masks, even when not selected for the online acquisition, a rate meter independently provides the corresponding trigger counting rate with a 1 s resolution. For each event passing the online trigger condition, the rate meters of each trigger mask are transmitted along with other scientific data, thus allowing the offline analysis for different particle selections and providing an estimation of the energy and angular dependencies.

As for previous space weather studies (Palma et al. 2021; Piersanti et al. 2022), these trigger-configuration rate meters have proven extremely helpful for GRB detection, as the online high-energy threshold configuration, T & P1 & P2, is useless due to the very low-energy particles involved in such phenomena, whereas the rate meter of a less deep configuration (such as T) exhibits a clear and significant response to transients of various physical nature.

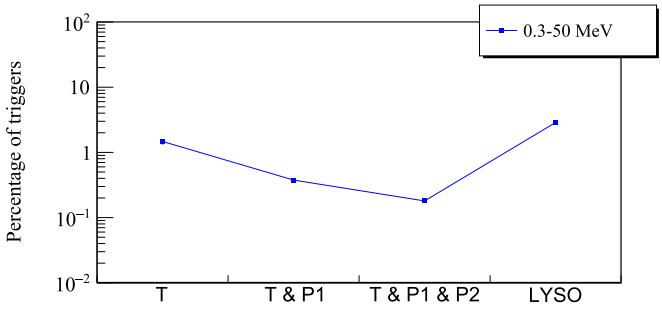


**Figure 2.** Percentage of triggers, estimated from Monte Carlo simulation, as a function of the trigger configuration in the photon energy interval 300 keV–50 MeV.

## 4. HEPD-01 as a Gamma-Ray Detector

In order to better assess the HEPD-01 capability to detect high-energy gamma-ray photons, a Monte Carlo simulation was performed using the official software developed by the CSES/Limadou Collaboration and based on a GEANT4 toolkit (Agostinelli et al. 2003). A sample of 100 million photons was isotropically generated according to a flat distribution in $\cos^2\theta$ ($0^{\circ} < \theta < 90^{\circ}$, $0^{\circ} < \Phi < 180^{\circ}$), and from a $40 \times 40$ $cm^2$ surface immediately above HEPD-01 particle entrance window. Finally, gamma rays were simulated according to a logarithmic energy distribution ranging from 300 keV to 50 MeV, in order to study the detector response over a wide energy interval. To estimate the percentage of triggers as a function of the trigger configuration, we counted the occurrences of charged particle formation (produced by the photons themselves) by requiring an energy deposition above the threshold for different combinations of subdetectors. Then, assuming a single interaction for each photon, we calculated the percentage as a ratio between this number and the initial number of gamma particles. Moreover, as LYSO crystals are usually employed as a valid instrument for low-energy electron and gamma detection, in this simulation we included not only the most superficial layers (T, P1, and P2) and their combinations but also a hypothetical configuration requiring only an above-threshold signal from the LYSO matrix. Indeed, a dedicated trigger mask including only the LYSO subdetector was not foreseen during the design phase of the trigger board and, thus, it is not currently implemented in HEPD-01. Figure 2 shows the percentage of triggers decreasing by a factor of $\sim$10 when passing from the T trigger mask to the T & P1 & P2 trigger mask. Indeed, as observed from in-flight rate meters, the trigger configurations, requiring the coincidence among above-threshold signals from the trigger plane and an increasing number of tower planes, are less and less efficient in detecting the low-energy secondary electrons, which are produced by the photon interactions. Conversely, even after passing through all the 16 tower planes, a significant fraction of photons interact in the dense high-$Z$ LYSO cubes, as clearly observed in Figure 2. This confirms the expected high efficiency of the LYSO matrix in detecting electrons and positrons from gamma-ray conversion despite the matrix being located at the bottom of the payload. For this reason, the second High-Energy Particle Detector (HEPD-02) will have a dedicated trigger system for gamma-ray detection through two planes of LYSO orthogonal bars. The Monte Carlo simulation results confirm that the mechanism in place, when high-energy photons illuminate the upmost section of the detector, is their interaction with the active (tracker silicon planes) and passive materials (aluminum

**Table 1**
Main Parameters for Each of the Five Selected GRBs

| GRB Identifier | R.A. (deg) | Decl. (deg) | Trigger Time (UTC) | HEPD-01 Duration (s) | Konus-Wind Fluence (0.3–50 MeV) (erg cm$^{-2}$) | HEPD-01 Fluence (0.3–50 MeV) (erg cm$^{-2}$) |
|---|---|---|---|---|---|---|
| GRB190114C | 56.2 | −31.8 | 20:57:03 | 6 | $(1.6 \pm 0.1) \times 10^{-4}$ | $(2.2 \pm 0.3) \times 10^{-4}$ |
| GRB190305A | 11.3 | −50.1 | 13:05:19 | 3 | $(1.2 \pm 0.3) \times 10^{-4}$ | $(1.0 \pm 0.3) \times 10^{-4}$ |
| GRB190928A | 36.6 | +29.5 | 13:13.48 | 11 | $(3.3 \pm 0.2) \times 10^{-4}$ | $(2.6 \pm 0.5) \times 10^{-3}$ |
| GRB200826B | 296.3 | +71.8 | 22:09:42 | 6 | $(1.1 \pm 0.1) \times 10^{-4}$ | $(3.0 \pm 0.5) \times 10^{-4}$ |
| GRB211211A | 211.3 | +27.1 | 13:59:09 | 9 | $(3.4 \pm 0.1) \times 10^{-4}$ | $(7.9 \pm 0.9) \times 10^{-4}$ |

structures, etc). This includes photoionization, Compton effect, and pair production, all generating secondary electrons with energies correlated to the primary gamma rays. Figure 3 shows the on-axis effective area of the instrument obtained with the trigger configuration used for the GRB data analysis.

The operative energy range is from 300 keV to 50 MeV, with peak efficiency at ∼2 MeV, and the actual on-axis effective area spans from ∼10 cm$^2$ at lower energy to ∼6 cm$^2$ at high energy. The energy resolution $\Delta E/E$, in the same trigger configuration, is intrinsically moderate due to the fact that the detector was designed to detect charged particles, vetoing photons.

The production of low-energy electrons triggered by the photon interaction in the upper sections of the HEPD-01 is clearly visible during the GRB light curve detection. The effect is the enhancement of the count rate recorded by the rate meter corresponding to trigger configuration T, which requires an above-threshold signal only in the trigger plane and allows the detection of the lowest energetic electrons (>3 MeV). Adding more tower planes in "AND" configuration with the counters of the trigger plane T suppresses the particle rate. This is why the rate meters of deeper trigger masks (such as T & P1, T & P1 & P2, and so on) do not show any increase in the GRB time.

## 5. Gamma-Ray Burst Observations

This paper reports the clear detection by HEPD-01 of five strong GRBs, via an electron-flux time profile which closely matches the time evolution of GRB photons mostly detected by dedicated gamma-ray detectors, in the energy range 1–1000 keV. HEPD-01 detections were limited to events with a fluence $>10^{-5}$ erg cm$^{-2}$ in the actual flight configuration optimized to reject photon triggers favoring charged particle ones. In Table 1 we report the fluence derived for each GRB in the HEPD-01 operative range 300 keV–50 MeV. Errors take into account a 20% contribution due to systematic uncertainties. The simultaneous light curves from GRB190114C, GRB190305A, GRB190928A, GRB200826B, and GRB211211A, reported in the literature, are very similar to the HEPD-01 ones, demonstrating a limited evolution of the spectral shape at higher energies, as will be discussed later.

### 5.1. Data Set

The entire HEPD-01 data set since the end of commissioning (2018 August) was analyzed in search for signals time-correlated with GRBs detected by gamma-ray instruments. We only considered GCNs reporting GRBs during periods when HEPD-01 was in operation and data were not affected by strong solar activity, the South Atlantic Anomaly passage, etc.

Relevant information on the five selected GRBs is given in Table 1. In columns 2 and 3, R.A. and decl., respectively, are the best positions from GCNs and literature; column 4 reports the trigger times from GCNs and literature; column 5 reports

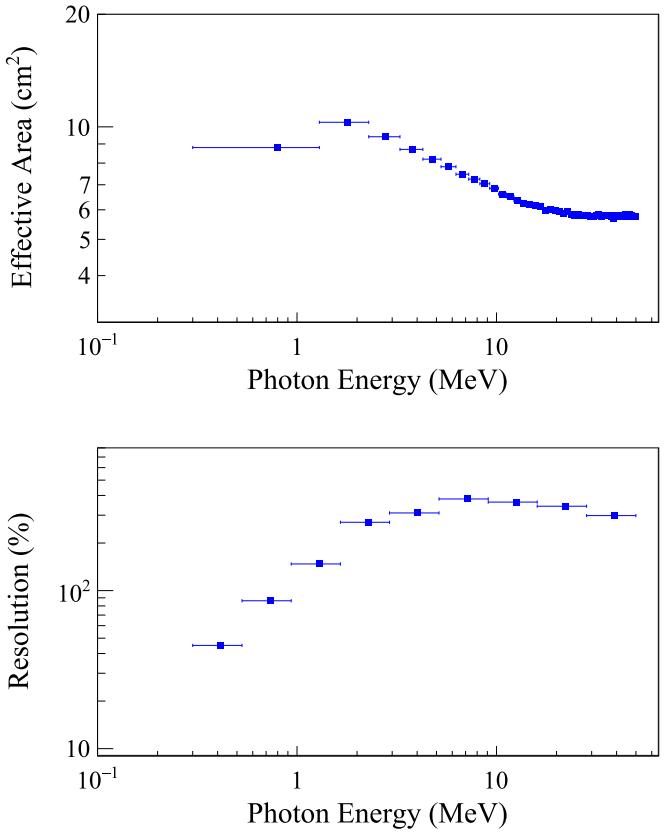


**Figure 3.** On-axis effective area (top panel) and energy resolution (bottom panel) of the HEPD-01 detector in the trigger configuration used for the GRB data analysis.

the $T_0$–$T_{90}$ duration from the HEPD-01 light curve. The recorded durations are lower than the ones reported in the GCNs for two reasons: (i) the bursts at high energy are usually shorter than at low energy; (ii) due to the moderate sensitivity of HEPD-01, the instrument triggers when the burst intensity is high enough to be statistically above the background level.

Details about each burst are reported in the following subsections.

### 5.2. GRB190114C

This GRB was the first detected at sub-TeV energy by MAGIC during prompt and afterglow phases (MAGIC Collaboration et al. 2019), after the first report at $T_0 = 20{:}57{:}03$ UTC by Swift-BAT (Gropp et al. 2019) in the 15–350 keV band ($T_{90} = 362$ s), and by Fermi Gamma-Ray Burst Monitor (GBM; Hamburg et al. 2019) in the 50–300 keV range ($T_{90} = 116$ s). The 10–1000 keV fluence reported by Fermi was $4.433 \times 10^{-4}$ erg cm$^{-2}$ (Ajello et al. 2020). The

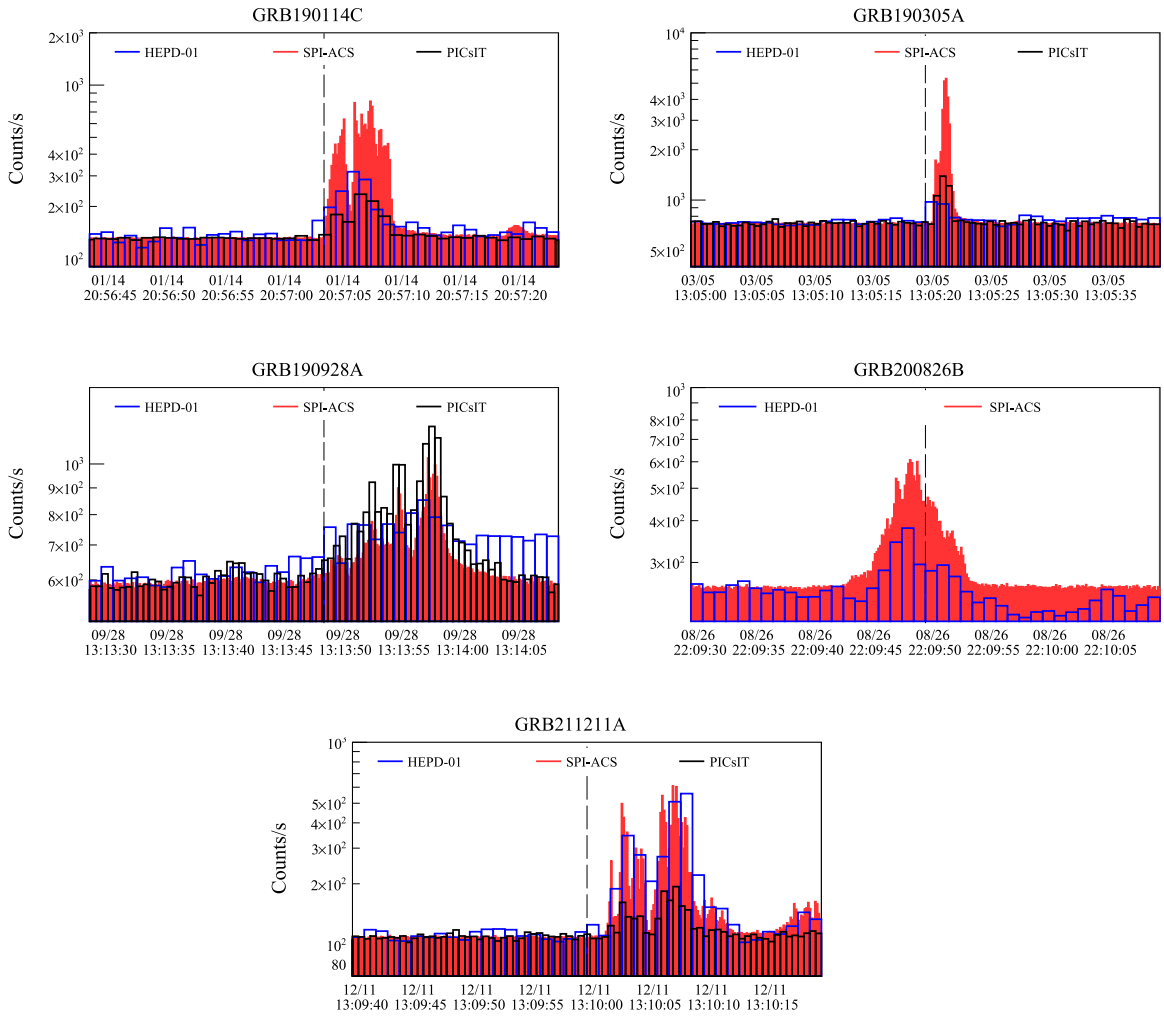


**Figure 4.** Time profiles of the low-energy electrons detected by the most superficial trigger configuration of HEPD-01—in blue—in comparison with the time profiles of the signals obtained from other instruments like PICsIT and SPI-ACS, in black and red, respectively. For better visualization, SPI-ACS and PICsIT data points are normalized to HEPD-01 ones. Each panel refers to a specific GRB. The vertical dashed line marks the trigger time $T_0$ for the start of each GRB.

redshift of the GRB is $z = 0.42$ (Selsing et al. 2019), which was used to estimate $E_{\rm iso} = 2.5 \times 10^{53}$ erg, where $E_{\rm iso}$ is the energy emitted in gamma rays, assuming that the emission is isotropic. Konus-Wind reported a 20 keV–10 MeV fluence of $(4.83 \pm 0.10) \times 10^{-4}$ erg cm$^{-2}$ (Frederiks et al. 2019a). Further information on the burst characteristics at optical wavelength is given in Melandri et al. (2022) via the monitoring between 1.3 and 370 days after the trigger, which revealed a supernova component (SN 2019jrj), underlying the GRB emission. The afterglow emission from this GRB was detected at various wave bands from 0.65 GHz to 23 GeV.

### 5.3. GRB190305A

This bright and long-duration GRB was first reported by Astro Rivelatore Gamma a Immagini Leggero (AGILE; Ursi et al. 2019a) at $T_0 = 13{:}05{:}19.34$ UTC, followed by Swift (Evans et al. 2019), Monitor of All-sky X-ray Image (Nakahira et al. 2019), Insight Hard X-ray Modulation Telescope (Insight-HXMT; Xiao et al. 2019), InterPlanetary Network (IPN) triangulation (Svinkin et al. 2021), and Konus-Wind (Kozlova et al. 2019). The fluence, as reported by Konus-Wind, was $1.47 \times 10^{-4}$ erg cm$^{-2}$.

### 5.4. GRB190928A

This bright and long GRB was first reported by AGILE (Ursi et al. 2019b) followed by the IPN triangulation (Hurley et al. 2019) and the Calorimetric Electron Telescope (Pal'Shin et al. 2019). The light curve showed multi-peaked pulses with periods of low emission. It was also detected by Konus-Wind (Frederiks et al. 2019b) for a total of about 195 s up to ∼15 MeV at fluence of $4.9 \times 10^{-4}$ erg cm$^{-2}$, including a 256 ms peak detected at $T_0 + 103$ s with a fluence of $9 \times 10^{-5}$ erg cm$^{-2}$ and peak energy of 591 keV. The burst was also reported by Insight-HXMT (Luo et al. 2019) and AstroSat (Gaikwad et al. 2019).

### 5.5. GRB200826B

First reported by the Fermi/GBM team (Malacaria et al. 2020) as an exceptionally bright and long GRB with $T_{90} = 7.4$ s in the 50–300 keV band, peak energy of 410 keV and fluence of $1.4 \times 10^{-4}$ erg cm$^{-2}$. The reported 20 keV–10 MeV fluence from Konus-Wind was $(2.0 \pm 0.1) \times 10^{-4}$ erg cm$^{-2}$ (Ridnaia et al. 2020). An IPN triangulation by Konus-Wind, INTEGRAL, and Mars-Odyssey was reported in Hurley et al. (2020). Konus-Wind (Ridnaia et al. 2020) showed a light curve with bright multipeak pulses of a total duration of 23 s and weak emission detected up to

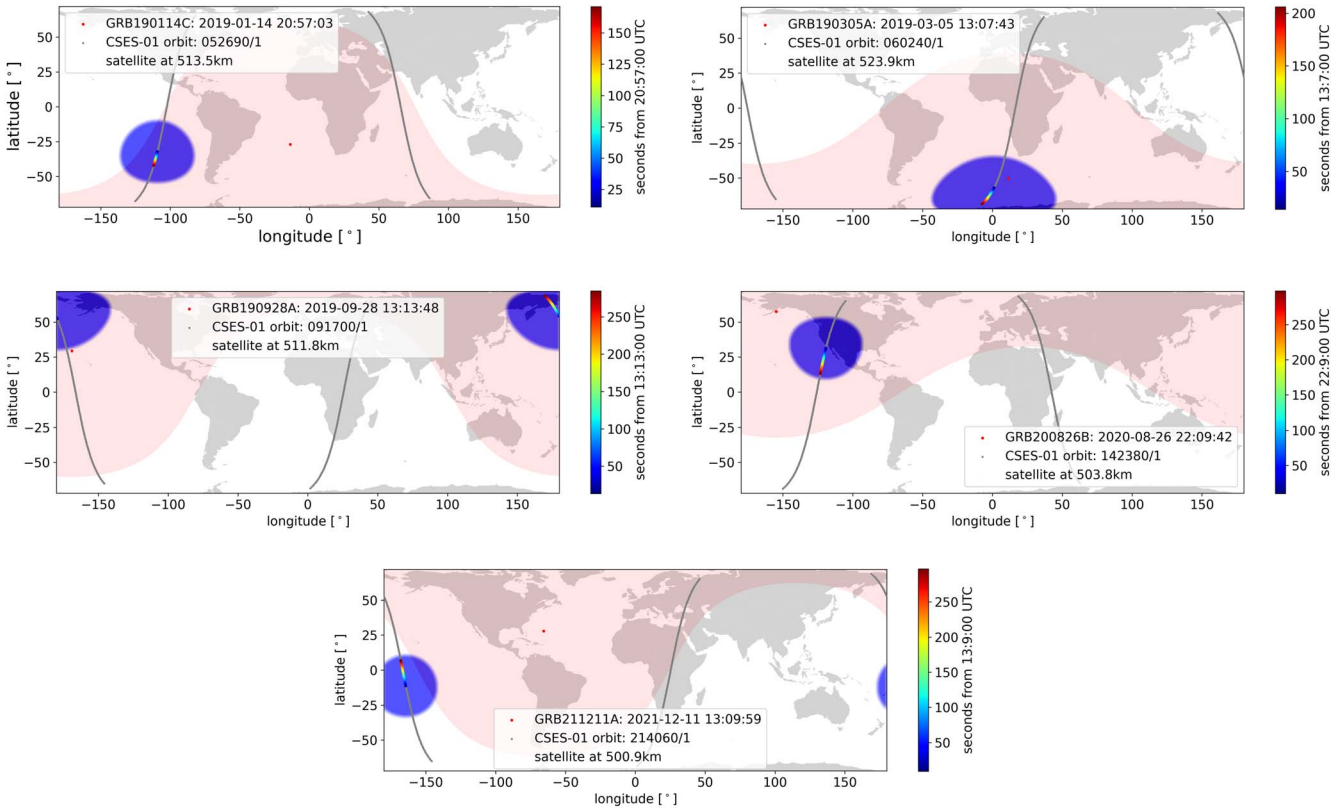


**Figure 5.** Five Earth maps (in correspondence with the observations shown in Figure 4) showing: the illuminated half-globe of the GRB (red area), the CSES-01 orbits close by in time (gray lines), and the horizon seen at the satellite altitude (given in the legend and shown as a blue area) at the moment of first impact of any GRB. The color bar reflects the time in seconds after the first GRB trigger and the corresponding position along the orbit.

$T_0 + 250$ s and 10 MeV, with a fluence of $2 \times 10^{-4}$ erg cm$^{-2}$ and peak energy of 337 keV.

### 5.6. GRB211211A

This enigmatic, hybrid GRB was reported by Swift as the second brightest and most complex up to that time (D'Ai et al. 2021) with emission extending up to $T_0 + 100$ s. Optical afterglow was promptly detected by Zheng & Filippenko (2021). A Swift fluence of $1.5 \times 10^{-4}$ erg cm$^{-2}$ (15–150 keV) was then reported in Stamatikos et al. (2021). Fermi/GBM showed a low-energy curve in the 10–300 keV range characterized by three separate pulses and a peak energy of 646.8 keV. The event fluence is $5.4 \times 10^{-4}$ erg cm$^{-2}$ (10–1000 keV) from $T_0$–1.264 s to $T_0 + 54.033$ s (Mangan et al. 2021). The optical, ultraviolet, and X-ray counterparts were immediately searched and finally a nearby host galaxy at a distance of 346 Mpc was identified by different authors. Further observations confirmed the initial GRB location and reported a peculiar slow decay associated with such a long GRB type (Malesani et al. 2021a). In Malesani et al. (2021b), Malesani corrected the $E_{\rm iso}$ value to $6.9 \times 10^{51}$ erg. The collected result from observational campaigns made clear the unusual nature of GRB211211A compared to the classical long GRBs at such a distance and suggested a generation mechanism from a compact binary merger (such as two neutron stars) in order to match location, rapid decay, and color (see Levan et al. 2021). The features of this event impacted the standard GRB scenario; characteristics, light curves, and new models are reported in Mei et al. (2022), Rastinejad et al. (2022), Troja et al. (2022), and Yang et al. (2022).

### 5.7. GRB Time Profiles and Detectability

In Figure 4 the time profiles of the low-energy (>3 MeV) electrons produced by the GRB-impinging photons and detected by the most superficial trigger configuration of HEPD-01, in blue, are compared with the time profiles of the signals obtained from dedicated gamma instruments. In this specific case, we used data from INTEGRAL/PICsIT (Labanti et al. 2003; Ubertini et al. 2003) and INTEGRAL/SPI-ACS (von Kienlin et al. 2003). For better visualization, SPI-ACS and PICsIT data points are normalized to HEPD-01 ones. The vertical dashed line appearing in each panel marks the $T_0$ trigger time reported by GCN for the start of the corresponding GRB. Although instruments like SPI-ACS and PICsIT have a higher resolution and are designed for this type of detection, the signals recorded by HEPD-01 show a good agreement in both shape and duration with previously reported observations, also providing a good enough timing resolution if compared to the one provided by PICsIT (7.9 or 15.8 ms depending on the observation period). Moreover, for each observed GRB, we estimated the significance of the detected signal over background: $50.7\sigma$ (GRB190114C), $17.6\sigma$ (GRB190305A), $83.8\sigma$ (GRB190928A), $24.9\sigma$ (GRB200826B), and $167.6\sigma$ (GRB211211A). We have compared the HEPD-01 (300 keV–50 MeV) measured fluence with the extrapolated fluence from the Konus-Wind Band model fits (20 keV–10 MeV). The ratios between the observed fluences and the expected ones are all greater than 1, apart for GRB190305A: 1.4 (GRB190114C), 0.8 (GRB190305A), 7.9 (GRB190928A), 2.7 (GRB200826B), and 2.3 (GRB211211A). The fluences are statistically compatible, within $2\sigma$, for GRB190114C and GRB190305A, while GRB190928A, GRB200826B, and GRB211211A are

incompatible with the extrapolation of the Konus-Wind spectra values. The higher fluxes could be due to a high-energy spectral component above 10 MeV, detected in GRB190928A, GRB200826B, and GRB211211A, as also observed in GRB190114C up to ∼100 MeV (Ursi et al. 2020). Finally, it is worth noting that the fluence of GRB190928A could be overestimated due to a change in the background rate during the detection, as can be seen in Figure 4. We have taken this variation into account, though there may be a systematic uncertainty larger than in the other cases.

Figure 5 shows the position of the CSES-01 satellite at the moment of the GRB impact, its illumination area estimated from the R.A. and decl. given in Table 1, and the satellite's horizon. The overlap between the red and blue areas confirms the visibility of the GRBs by the instruments on board the satellite, which is confirmed for all five GRBs discussed above.

## 6. Conclusions

The serendipitous detection of five GRBs by the HEPD-01 detector in the energy range 300 keV–50 MeV has provided additional information on a set of strong events with a typical fluence above $\sim 3 \times 10^{-5}$ erg cm$^{-2}$, which corresponds to the $2\sigma$ detection limit of HEPD-01 in the trigger configuration running during the reported GRB observation. In particular, the high-energy extension up to 50 MeV, additional coverage, and duty cycle thanks to the polar orbit, high time resolution, and positional accuracy of the CSES-01 satellite position provide a valuable contribution to the single GRB characterization.

The reported results show how a light and compact payload with a similar design to HEPD-01's (e.g., HEPD-02) can detect extreme astrophysical phenomena like GRBs, and how the presence of LYSO will be crucial for this kind of physics. Furthermore, given the fast response of the detector and the instrumental upgrades in HEPD-02, the participation of the mission in a wider, real-time alert program (IPN, etc.), is foreseen during the second mission.

The reported GRB observation by HEPD-01 is valuable per se, as an independent source of data, given the 5 yr uninterrupted observations, all-sky sensitivity (aside from the Earth obscuration), high-energy extended response, and considering the forthcoming launch of HEPD-02 (De Santis & Ricciarini 2021) on board the CSES-02 satellite. The second-generation HEPD-02 detector has a dedicated trigger system to detect photons interacting with the plastic scintillator range calorimeter, providing a peak sensitive area of ∼30 cm$^2$ at 2 MeV (Lega et al. 2023), and with the LYSO bulk scintillators featuring an area of ∼150 cm$^2$ between 5 and 50 MeV (Follega 2023).

## Acknowledgments

This work makes use of data from the CSES mission, a project funded by the China National Space Administration (CNSA), China Earthquake Administration (CEA) in collaboration with the Italian Space Agency (ASI), National Institute for Nuclear Physics (INFN), Institute for Applied Physics (IFAC-CNR), and Institute for Space Astrophysics and Planetology (INAF-IAPS). This work was supported by the Italian Space Agency in the framework of the "Accordo Attuativo 2020-32.HH.0 Limadou Scienza+" (CUP F19C20000110005), the ASI-INFN Agreement No. 2014-037-R.0, addendum 2014-037-R-1-2017, and the ASI-INFN Agreement No. 2021-43-HH.0. A.B., J.C.R., P.U., and U.Z. acknowledge the Italian Space Agency for the financial support under the INTEGRAL ASI-INAF agreement No. 2019-35-HH.0.

## ORCID iDs

F. Palma https://orcid.org/0000-0001-7076-8830
M. Martucci https://orcid.org/0000-0002-3033-4824
C. Neubüser https://orcid.org/0000-0002-2008-8404
A. Sotgiu https://orcid.org/0000-0001-8835-2796
F. M. Follega https://orcid.org/0000-0003-2317-9560
P. Ubertini https://orcid.org/0000-0003-0601-0261
A. Bazzano https://orcid.org/0000-0002-2017-4396
J. C. Rodi https://orcid.org/0000-0003-2126-5908
R. Ammendola https://orcid.org/0000-0003-4501-3289
D. Badoni https://orcid.org/0000-0002-9027-2039
S. Bartocci https://orcid.org/0000-0002-3066-8621
R. Battiston https://orcid.org/0000-0002-5808-7239
S. Beolè https://orcid.org/0000-0003-4673-8038
I. Bertello https://orcid.org/0000-0002-5260-416X
W. J. Burger https://orcid.org/0000-0003-1977-6354
D. Campana https://orcid.org/0000-0003-1504-9707
A. Cicone https://orcid.org/0000-0002-8107-9624
S. Coli https://orcid.org/0000-0001-7470-4463
L. Conti https://orcid.org/0000-0003-2966-2000
A. Contin https://orcid.org/0000-0002-2535-5700
M. Cristoforetti https://orcid.org/0000-0002-0127-1342
G. D'Angelo https://orcid.org/0000-0002-9214-2051
C. De Donato https://orcid.org/0000-0002-9725-1281
C. De Santis https://orcid.org/0000-0002-7280-2446
P. Diego https://orcid.org/0000-0001-8279-020X
A. Di Luca https://orcid.org/0000-0002-9074-2133
G. Gebbia https://orcid.org/0000-0001-7252-7416
R. Iuppa https://orcid.org/0000-0001-5038-2762
A. Lega https://orcid.org/0000-0002-1660-0524
G. Masciantonio https://orcid.org/0000-0002-8911-1561
M. Mese https://orcid.org/0000-0003-1452-3542
F. Nozzoli https://orcid.org/0000-0002-4355-7947
A. Oliva https://orcid.org/0000-0002-6612-6170
G. Osteria https://orcid.org/0000-0002-9871-8103
F. Palmonari https://orcid.org/0000-0003-3707-0013
B. Panico https://orcid.org/0000-0003-1063-6961
E. Papini https://orcid.org/0000-0002-7969-7415
A. Parmentier https://orcid.org/0000-0002-9073-3288
S. Perciballi https://orcid.org/0000-0003-2868-2819
A. Perinelli https://orcid.org/0000-0001-5603-3950
P. Picozza https://orcid.org/0000-0002-7986-3321
M. Piersanti https://orcid.org/0000-0001-5207-2944
M. Pozzato https://orcid.org/0000-0003-0279-5436
G. Rebustini https://orcid.org/0000-0001-8587-592X
D. Recchiuti https://orcid.org/0000-0002-9530-6779
E. Ricci https://orcid.org/0000-0002-4222-9976
M. Ricci https://orcid.org/0000-0001-6816-4894
S. B. Ricciarini https://orcid.org/0000-0001-6176-3368
A. Russi https://orcid.org/0000-0001-7884-2310
Z. Sahnoun https://orcid.org/0000-0003-1176-2003
U. Savino https://orcid.org/0000-0003-1884-2444
V. Scotti https://orcid.org/0000-0003-3253-2805
R. Sparvoli https://orcid.org/0000-0002-6314-6117
S. Tofani https://orcid.org/0000-0002-0839-955X
V. Vilona https://orcid.org/0000-0001-9893-9419
V. Vitale https://orcid.org/0000-0001-8040-7852
U. Zannoni https://orcid.org/0000-0002-6657-8193
P. Zuccon https://orcid.org/0000-0001-6132-754X

## References


Abbott, B. P., Abbott, R., Abbott, T. D., et al. 2017a, PhRvL, 119, 161101
Abbott, B. P., Abbott, R., Abbott, T. D., et al. 2017b, ApJL, 848, L13
Agostinelli, S., Allison, J., Amako, K., et al. 2003, NIMPA, 506, 250
Ajello, M., Arimoto, M., Axelsson, M., et al. 2020, ApJ, 890, 9
Ambrosi, G., Bartocci, S., Basara, L., et al. 2020, NIMPA, 974, 164170
Ambrosi, G., Bartocci, S., Basara, L., et al. 2021, NIMPA, 1013, 165639
Band, D., Matteson, J., Ford, L., et al. 1993, ApJ, 413, 281
Bartocci, S., Battiston, R., Burger, W. J., et al. 2020, ApJ, 901, 8
Battiston, R., Neubüser, C., Follega, F. M., et al. 2023, ApJL, 946, L29
Burns, E., Svinkin, D., Fenimore, E., et al. 2023, ApJL, 946, L31
Burns, E., Svinkin, D., Hurley, K., et al. 2021, ApJL, 907, L28
Campana, S., Ghirlanda, G., Salvaterra, R., et al. 2022, NatAs, 6, 1101
Cano, Z., Wang, S.-Q., Dai, Z.-G., & Wu, X.-F. 2017, AdAst, 2017, 8929054
Costa, E., Frontera, F., Heise, J., et al. 1997, Natur, 387, 783
D'Ai, A., Ambrosi, E., D'Elia, V., et al. 2021, GCN, 31202
De Santis, C., & Ricciarini, S. 2021, ICRC (Berlin), 395, 058
Dezalay, J. P., Barat, C., Talon, R., et al. 1991, in AIP Conf. Ser. 265, Gamma-Ray Bursts (Melville, NY: AIP), 304
Evans, P. A. 2019, GCN, 23931
Fishman, G. J. 2013, in Gamma-ray Bursts: 15 Years of GRB Afterglows – Progenitors, Environments and Host Galaxies from the Nearby to the Early Universe, ed. A. J. Castro-Tirado et al., 61 (EAS, EDP Sciences), 5
Follega, F. M. 2023, ICRC (Nagoya), 444, 116
Frederiks, D., Golenetskii, S., Aptekar, R., et al. 2019a, GCN, 23737
Frederiks, D., Golenetskii, S., Aptekar, R., et al. 2019b, GCN, 25868
Gaikwad, R., Sharma, V., Bhattacharya, D., et al. 2019, GCN, 25965
Galama, T. J., Vreeswijk, P. M., van Paradijs, J., et al. 1998, Natur, 395, 670
Gehrels, N., Chincarini, G., Giommi, P., et al. 2004, ApJ, 611, 1005
Goldstein, A., Veres, P., Burns, E., et al. 2017, ApJL, 848, L14
Gropp, J. D., Kennea, J. A., Klingler, N. J., et al. 2019, GCN, 23688, 1
Hamburg, R., Veres, P., Meegan, C., et al. 2019, GCN, 23707, 1
Huang, Y., Hu, S., Chen, S., et al. 2022, GCN, 32677, 1
Hurley, K., Mitrofanov, I. G., Golovin, D. V., et al. 2020, GCN, 28303
Hurley, K., Mitrofanov, I. G., Golovin, D. V., et al. 2019, GCN, 25864
Klebesadel, R. W., Strong, I. B., & Olson, R. A. 1973, ApJL, 182, L85
Kouveliotou, C., Meegan, C. A., Fishman, G. J., et al. 1993, ApJL, 413, L101
Kozlova, A., Golenetskii, S., Aptekar, R., et al. 2019, GCN, 23939
Labanti, C., Di Cocco, G., Ferro, G., et al. 2003, A&A, 411, L149
Lega, A., Follega, F., Iuppa, R., et al. 2023, ICRC (Nagoya), 444, 758
Levan, A. J., Rastinejad, J., Gompertz, B., et al. 2021, GCN, 31235
Luo, Q., Cai, C., Xiao, S., et al. 2019, GCN, 25879
MAGIC Collaboration, Acciari, V. A., Ansoldi, S., et al. 2019, Natur, 575, 455
Malacaria, C., Meegan, C. & Fermi GBM Team 2020, GCN, 28298
Malesani, D. B., Fynbo, J. P. U., de Ugarte Postigo, A., et al. 2021a, GCN, 31221
Malesani, D. B. 2021b, GCN, 31223
Mangan, J., Dunwoody, R., & Meegan, C. 2021, GCN, 31210
Martucci, M., Ammendola, R., Badoni, D., et al. 2023, ApJL, 945, L39
Martucci, M., Bartocci, S., Battiston, R., et al. 2022, PhRvD, 105, 062001
Martucci, M., Laurenza, M., Benella, S., et al. 2023, SpWea, 21, e2022SW003191
Mazets, E. P., Aptekar, R. L., Cline, T. L., et al. 2008, ApJ, 680, 545
Mazets, E. P., Golenetskii, S., Ilyinskii, V. N., et al. 1981, Ap&SS, 80, 119
Mazets, E. P., Golentskii, S. V., Ilinskii, V. N., Aptekar, R. L., & Guryan, I. A. 1979, Natur, 282, 587
Mei, A., Banerjee, B., Oganesyan, G., et al. 2022, Natur, 612, 236
Melandri, A., Izzo, L., Pian, E., et al. 2022, A&A, 659, A39
Mereghetti, S., Götz, D., Borkowski, J., Walter, R., & Pedersen, H. 2003, A&A, 411, L291
Nakahira, S., Sugita, S., Iwakiri, W., et al. 2019, GCN, 23933
Palma, F., Sotgiu, A., Parmentier, A., et al. 2021, Appl. Sci., 11, 5680
Pal'Shin, V., Yoshida, A., Sakamoto, T., et al. 2019, GCN, 25865
Picozza, P., Battiston, R., Ambrosi, G., et al. 2019, ApJS, 243, 16
Piersanti, M., Del Moro, D., Parmentier, A., et al. 2022, SpWea, 20, e2021SW003016
Rastinejad, J. C., Gompertz, B. P., Levan, A. J., et al. 2022, Natur, 612, 223
Ridnaia, A., Golenetskii, S., Aptekar, R., et al. 2020, GCN, 28304
Rodi, J., & Ubertini, P. 2023, A&A, 677, L3
Savchenko, V., Ferrigno, C., Kuulkers, E., et al. 2017, ApJL, 848, L15
Schösser, E. C., Burgess, J. M., & Greiner, J. 2023, arXiv:2303.05922
Selsing, J., Fynbo, J. P. U., Heintz, K. E., & Watson, D. 2019, GCN, 23695
Shen, X., Zhang, X., Yuan, S., et al. 2018, Sci. China: Technol. Sci., 61, 634
Sotgiu, A., De Donato, C., Fornaro, C., et al. 2020, Software: Pract. Exper., 51, 1459
Stamatikos, M., Barthelmy, S. D., D'Ai, A., et al. 2021, GCN, 31209
Svinkin, D., Frederiks, D., Hurley, K., et al. 2021, Natur, 589, 211
Svinkin, D., Golenetskii, S., Aptekar, R., et al. 2021, GCN, 23936
Troja, E., Fryer, C. L., O'Connor, B., et al. 2022, Natur, 612, 228
Ubertini, P., Bazzano, A., Natalucci, L., et al. 2019, RLSFN, 30, 65
Ubertini, P., Lebrun, F., Di Cocco, G., et al. 2003, A&A, 411, L131
Ursi, A., Tavani, M., Frederiks, D. D., et al. 2020, ApJ, 904, 133
Ursi, A., Cardillo, M., Casentini, C., et al. 2019a, GCN, 23930
Ursi, A., Tavani, M., Cardillo, M., et al. 2019b, GCN, 25859
van Paradijs, J., Groot, P. J., Galama, T., et al. 1997, Natur, 386, 686
von Kienlin, A., Beckmann, V., Rau, A., et al. 2003, A&A, 411, L299
Winkler, C., Courvoisier, T. J.-L., Di Cocco, G., et al. 2003, A&A, 411, L1
Xiao, S., Li, C. K., Li, X. B., et al. 2019, GCN, 23934
Yang, J., Ai, S., Zhang, B.-B., et al. 2022, Natur, 612, 232
Zheng, W., & Filippenko, A. V. 2021, GCN, 31203